Optical properties of AFe$_2$As$_2$ (A=Ca, Sr, and Ba) single crystals

Y. M. Dai,[1,*] Ana Akrap,[2] S. L. Bud'ko,[3] P. C. Canfield,[3] and C. C. Homes[1,†]

[1]*Condensed Matter Physics and Materials Science Division, Brookhaven National Laboratory, Upton, New York 11973, USA*
[2]*DQMP–University of Geneva, CH-1211 Geneva 4, Switzerland*
[3]*Ames Laboratory, U.S. DOE, and Department of Physics and Astronomy, Iowa State University, Ames, Iowa 50011, USA*

The detailed optical properties have been determined for the iron-based materials AFe$_2$As$_2$, where $A = $ Ca, Sr, and Ba, for light polarized in the iron-arsenic (a-b) planes over a wide frequency range, above and below the magnetic and structural transitions at $T_N = 138$, 195, and 172 K, respectively. The real and imaginary parts of the complex conductivity are fit simultaneously using two Drude terms in combination with a series of oscillators. Above T_N, the free-carrier response consists of a weak, narrow Drude term, and a strong, broad Drude term, both of which show only a weak temperature dependence. Below T_N there is a slight decrease of the plasma frequency but a dramatic drop in the scattering rate for the narrow Drude term, and for the broad Drude term there is a significant decrease in the plasma frequency, while the decrease in the scattering rate, albeit significant, is not as severe. The small values observed for the scattering rates for the narrow Drude term for $T \ll T_N$ may be related to the Dirac conelike dispersion of the electronic bands. Below T_N new features emerge in the optical conductivity that are associated with the reconstruction Fermi surface and the gapping of bands at $\Delta_1 \simeq 45$–80 meV, and $\Delta_2 \simeq 110$–210 meV. The reduction in the spectral weight associated with the free carriers is captured by the gap structure; specifically, the spectral weight from the narrow Drude term appears to be transferred into the low-energy gap feature, while the missing weight from the broad term shifts to the high-energy gap.

I. INTRODUCTION

The discovery of the iron-based superconductors has resulted in an intensive investigation of this class of materials in the hope of discovering new compounds with high superconducting critical temperatures (T_c's) [1–4]. The iron-arsenic materials are characterized by Fe-As sheets separated by layers of different elements or chemical structures. One material, BaFe$_2$As$_2$, is particularly useful as superconductivity can be induced by the application of pressure [5–8], as well as electron [9–12], hole [13–15], or isovalent doping [16–19], with T_c's as high as 40 K in the hole-doped material. At room temperature, BaFe$_2$As$_2$ is a paramagnetic metal with a tetragonal structure. The resistivity in the planes decreases with temperature until it drops anomalously as the material undergoes a magnetic transition at $T_N \simeq 138$ K to a spin-density-wave (SDW) -like antiferromagnetic ground state that is also accompanied by a structural transition to an orthorhombic phase [20–22]. The resistivity also displays a slight anisotropy close to and below T_N, being slightly larger along the b axis than along a [23]; however, this anisotropy decreases dramatically if the samples are annealed [24]. The related materials CaFe$_2$As$_2$ and SrFe$_2$As$_2$ have similar transport properties due to magnetic and structural transitions that occur at $T_N \simeq 172$ and 195 K, respectively [25–30].

The broad interest in this family of materials has resulted in a number of optical studies [31–41]. Early investigations treated the free-carrier response using only a single band. However, a minimal description of the electronic structure of the iron-arsenic materials consists of hole and electron pockets at the center and corners of the Brillouin zone,

respectively [42,43]. As a result, more recent studies consider a two band approach (the so-called two-Drude model) in which the electron and hole pockets are treated as separate electronic subsystems [44]. Above T_N, this model reveals the presence of a narrow Drude response that has a strong temperature dependence in combination with a broad Drude term that is essentially temperature independent. Below T_N, the optical conductivity undergoes dramatic changes due to the reconstruction of the Fermi surface [45–51]; however, one of the most detailed optical studies on this family of materials restricts the two-Drude analysis to $T \gtrsim T_N$ [39].

In this study the detailed temperature dependence of the complex optical properties in the a-b planes of single crystals of BaFe$_2$As$_2$, SrFe$_2$As$_2$, and CaFe$_2$As$_2$, have been determined above and below T_N. This allows the evolution of the electronic properties and the SDW gaplike features ($T < T_N$) with the different alkaline-earth-metal atoms to be tracked. The complex conductivity has been modeled using the two-Drude model. Above T_N, the complex conductivity is described by a strong, broad Drude response, and a narrow, less intense term, both of which exhibit only a weak temperature dependence, in combination with a strong interband feature at about 0.5 eV; these results are in good agreement with other works. Below T_N, there is a dramatic narrowing of the Drude responses and a suppression of the low-frequency conductivity as spectral weight is transferred to two new gaplike features that appear below about 200 meV. To avoid the difficulties of false convergence typically associated with the extra degrees of freedom due to these new gap features, we introduce the constraint that the spectral weight due to the Drude terms above T_N must be captured by the Drude terms and the two oscillators used to describe the gap features below T_N. Using this approach, reliable convergence is achieved and we are able to track the detailed temperature dependence of the Drude and Lorentz parameters below T_N.
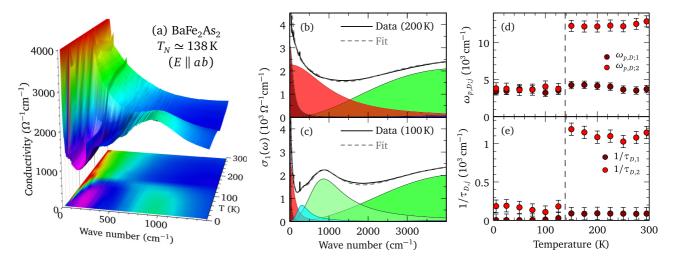
---

*ymdai@lanl.gov
†homes@bnl.gov

FIG. 1. (a) The temperature dependence of the real part of the optical conductivity for light polarized in the a-b planes of BaFe$_2$As$_2$ above and below $T_N = 138$ K showing the dramatic redistribution of spectral weight below T_N. The results of the fits to the complex conductivity are compared to the real part of the conductivity at (b) 200 K, and (c) 100 K; the fit is decomposed into the contributions from the narrow and broad Drude components, as well as several of the Lorentz oscillators. The temperature dependence of the (d) plasma frequencies and (e) scattering rates for the broad and narrow Drude components above and below T_N.

We observe the same response in all three materials; namely, just below T_N there is a slight reduction of the plasma frequency for the narrow term, but a dramatic decrease of the scattering rate, while for the broad Drude term there is a significant reduction of both the plasma frequency and the scattering rate. The missing spectral weight in the narrow Drude term appears to be transferred to the low-energy gap feature ($\Delta_1 \simeq 45$–80 meV), while the missing weight from the broad Drude term appears to be transferred to the high-energy gap ($\Delta_2 \simeq 110$–210 meV). We also note that the increasing values for the plasma frequencies and the gap values are scaling roughly with the electron affinities of the alkaline-earth-metal atoms.

II. EXPERIMENT

Single crystals of AFe$_2$As$_2$ (A = Ba, Sr, or Ca) were grown using conventional high-temperature solution growth techniques either out of self-flux (A = Ba) [10], or out of Sn flux (A = Sr, Ca) [52,53] and characterized by scattering and bulk physical measurements. These crystals have not been annealed.

The reflectance of millimeter-sized, as-grown crystal faces has been measured at a near-normal angle of incidence for light polarized in the a-b planes over a wide frequency range from the far infrared ($\simeq 2$ meV) to the ultraviolet ($\simeq 4$–5 eV) for a wide variety of temperatures above and below T_N using an *in situ* evaporation technique [54]. The complex optical conductivity has been determined from a Kramers-Kronig analysis of the reflectance [55], which requires extrapolations for $\omega \to 0, \infty$. At low frequency, the material is always metallic, so the Hagen-Rubens form for the reflectance is employed, $R(\omega) = 1 - a\sqrt{\omega}$, where a is chosen to match the data at the lowest-measured frequency point. Above the highest-measured frequency, the reflectance is typically assumed to be constant up to 8×10^4 cm^{-1}, above which a

free-electron gas asymptotic reflectance extrapolation $R(\omega) \propto 1/\omega^4$ is assumed [56].

III. RESULTS AND DISCUSSION

For simplicity, the multiple hole and electron bands are gathered into single electron and hole pockets that are treated as two separate electronic subsystems using the so-called two-Drude model [44] with the complex dielectric function $\tilde{\epsilon} = \epsilon_1 + i\epsilon_2$,

$$\tilde{\epsilon}(\omega) = \epsilon_\infty - \sum_{j=1}^{2} \frac{\omega_{p,D;j}^2}{\omega^2 + i\omega/\tau_{D,j}} + \sum_k \frac{\Omega_k^2}{\omega_k^2 - \omega^2 - i\omega\gamma_k},$$

(1)

where ϵ_∞ is the real part at high frequency. In the first sum $\omega_{p,D;j}^2 = 4\pi n_j e^2/m_j^*$ and $1/\tau_{D,j}$ are the square of the plasma frequency and scattering rate for the delocalized (Drude) carriers in the jth band, respectively, and n_j and m_j^* are the carrier concentration and effective mass. In the second summation, ω_k, γ_k, and Ω_k are the position, width, and strength of the kth vibration or bound excitation. The complex conductivity is $\tilde{\sigma}(\omega) = \sigma_1 + i\sigma_2 = -2\pi i\omega[\tilde{\epsilon}(\omega) - \epsilon_\infty]/Z_0$ (in units of Ω^{-1} cm^{-1}); $Z_0 \simeq 377$ Ω is the impedance of free space.

A. BaFe$_2$As$_2$

The temperature dependence of the real part of the optical conductivity of BaFe$_2$As$_2$ for light polarized in the a-b planes is shown in Fig. 1(a) in the infrared region. Above T_N, the conductivity is metallic with a Drude-like free-carrier component that slowly gives way with increasing frequency to a series of interband transitions (the reflectance and the optical conductivity are shown over a broader energy range in Figs. S1 and S2 in the Supplemental Material [57]). Below T_N, a narrow free-carrier response is observed at low frequency and there is a dramatic suppression of the conductivity in the far-infrared

region with a commensurate transfer of spectral weight to the peaks that emerge at $\simeq 360$ and 900 cm^{-1}. The spectral weight is defined as the area under the conductivity curve over a given interval,

$$S(\omega) = \int_0^\omega \sigma_1(\omega')d\omega'. \qquad (2)$$

These results are in good agreement with other optical studies of this material [31–40].

The real and imaginary parts of the complex optical conductivity have been fit simultaneously with the Drude-Lorentz model using a nonlinear least-squares technique. For $T > T_N$, the data was initially fit using a single Drude component and a series of Lorentzian oscillators to reproduce the interband transitions; however, even with extremely overdamped oscillators, the returned fits were of poor quality. A low-frequency Lorentz oscillator was introduced to improve the quality of the fit; however, the best result was obtained when the frequency of this oscillator went to zero and a second Drude component was recovered. Given the multiband nature of this material, this is a natural result. While there are as many as five Fermi surfaces, we have adopted a minimal description that only considers two sets of carriers; this approach has the advantage of producing good fits, as well as keeping the total number of parameters (degrees of freedom) relatively low, an approach that typically results in fits with good convergence.

The fit to the real part of the optical conductivity using the two-Drude model above T_N at 200 K is shown in Fig. 1(b) where the individual Drude and Lorentz contributions are shown. The data is reproduced quite well by a narrow and a broad Drude term, with $\omega_{p,D;1} \simeq 4200$ cm^{-1} and $1/\tau_{D,1} \simeq 90$ cm^{-1}, and $\omega_{p,D;2} \simeq 12\,200$ cm^{-1} and $1/\tau_{D,2} \simeq 1100$ cm^{-1}, respectively, as well as bound excitations at $\omega_1 \simeq 4450$ cm^{-1} and $\omega_2 \simeq 13\,800$ cm^{-1}, which are attributed to interband transitions [58,59]; the parameters for the Drude components, as well as the first two Lorentzian oscillators, are listed in Table I(a). The observation of narrow and broad terms in the two-Drude analysis is in agreement with other optical studies [37–40], and appears to be a general result for most of the iron-based materials that incorporate iron-arsenic sheets. If the plasma frequencies for the free carriers are added in quadrature [Eq. (3)], then the derived plasma frequency $\omega_p \simeq 12\,900$ cm^{-1} is in good agreement with a previous study on this material that considered only a single Drude component [31].

This approach has also been applied to the optical conductivity below T_N, where two new oscillators at $\omega_{01} \simeq 360$ cm^{-1} and $\omega_{02} \simeq 900$ cm^{-1} have been included to reproduce the broad peaks that emerge in the optical conductivity at low temperature. However, the six extra degrees of freedom introduced by the two new oscillators can lead to a false convergence with nonunique solutions. By observing that the loss of spectral weight of the free carriers below T_N appears to be captured by the two new oscillators, we can introduce the constraint that the redistribution of the spectral weight among these fitted parameters must be a conserved quantity. This is equivalent to the statement that below $\simeq 5000$ cm^{-1} the spectral weight is roughly constant. Thus, above and

below T_N,

$$\omega_p \simeq \begin{cases} \sqrt{\omega_{p,D;1}^2 + \omega_{p,D;2}^2} & (T > T_N) \\ \sqrt{\omega_{p,D;1}^2 + \omega_{p,D;2}^2 + \Omega_{01}^2 + \Omega_{02}^2} & (T < T_N), \end{cases} \qquad (3)$$

where Ω_{01} and Ω_{02} are the strengths of the two new oscillators; this constraint leads unique solutions (this is explored in more detail in the Supplemental Material). The results of the fit to the data at 100 K using this approach are shown in Fig. 1(c); the Drude components have narrowed and lost spectral weight, which has shifted to the two new oscillators; the excitation ω_1 has shifted upwards slightly to $\simeq 4600$ cm^{-1}, but otherwise shows relatively little temperature dependence below T_N [Table I(a)]. These results are in good agreement with the optical conductivity of a detwinned sample at 5 K [37], which show that the broad Drude component is only observed along the a axis, while the narrow Drude component is observed in both the a and the b directions. The fact that the narrow Drude component is isotropic suggests that it is not related to the magnetic order in this material.

The temperature dependence of the plasma frequencies and scattering rates for the two Drude components are shown in Figs. 1(d) and 1(e), respectively; above T_N the parameters are essentially temperature independent, which is not surprising given the weak temperature dependence of the optical conductivity. Below T_N, the plasma frequency for the broad Drude component decreases dramatically from $\omega_{p,D;2} \simeq 12\,300 \rightarrow 3800$ cm^{-1}, while the plasma frequency for the narrow component decreases only slightly, $\omega_{p,D;1} \simeq 4200 \rightarrow 3400$ cm^{-1}. The total carrier concentration is observed to decrease from $\omega_{p,D} \simeq 12\,900 \rightarrow 5100$ cm^{-1}. This roughly 85% decrease in the number of free carriers is in agreement with previous estimates [31,32]. The values for the plasma frequencies of the narrow and broad Drude components, and the intensities of the two new oscillators obey the constraint in Eq. (3), with $\omega_p \simeq 13\,200 \pm 500$ cm^{-1} ($T \ll T_N$). A closer examination of the values returned from the fits reveals that the missing spectral weight from the narrow Drude component appears to be captured by ω_{01},

$$\omega_{p,D;1}^2(T \gtrsim T_N) \simeq \omega_{p,D;1}^2(T \ll T_N) + \Omega_{01}^2, \qquad (4)$$

and likewise the loss of spectral weight from the broad Drude component appears to be captured by ω_{02},

$$\omega_{p,D;2}^2(T \gtrsim T_N) \simeq \omega_{p,D;2}^2(T \ll T_N) + \Omega_{02}^2. \qquad (5)$$

Allowing that the Fermi surface reconstruction below T_N results in the partial gapping of the two pockets, it is reasonable to associate ω_{01} and ω_{02} with gaplike features in the optical conductivity that appear to be more or less isotropic in the a-b planes [37,60]. The average optical gap for the narrow Drude band is therefore estimated to be $\Delta_1 \simeq 44$ meV, while for the broad Drude band it is $\Delta_2 \simeq 112$ meV. These estimates are in good agreement with the peaks observed in the Raman response [61] and the optical conductivity [31,39], as well as the values for Δ_1 and Δ_2 determined from them (in this work the average value for the gap is always associated with the peak in the conductivity).

TABLE I. The results of the nonlinear least-squares fit of the two-Drude model with Lorentz oscillators to the complex conductivity of $BaFe_2As_2$, $SrFe_2As_2$, and $CaFe_2As_2$ at all measured temperatures. The terms D_1 and D_2 denote the two Drude contributions, while L_1 and L_2 are the two low-frequency Lorentzian oscillators; the two new oscillators that appear below T_N are denoted L_{01} and L_{02}. The oscillators above 0.5 eV display relatively little temperature dependence. The estimated errors for the location and width are typically 2% or less, and 5% or less for the plasma frequency (oscillator strength). All units are in cm^{-1} unless otherwise indicated. A convenient conversion is 1 eV = 8065.5 cm^{-1}.

(a) $BaFe_2As_2$ ($T_N \simeq 138\,K$)

	D_1		D_2		L_{01}			L_{02}			L_1			L_2^a		
T (K)	$1/\tau_{D,1}$	$\omega_{p,D;1}$	$1/\tau_{D,2}$	$\omega_{p,D;2}$	ω_{01}	γ_{01}	Ω_{01}	ω_{02}	γ_{02}	Ω_{02}	ω_1	γ_1	Ω_1	ω_2	γ_2	Ω_2
295	88	3717	1143	12870							4222	8883	33260	13745	19380	21710
275	85	3535	1080	12530							4278	8920	32981	13863	19443	21678
250	88	3654	1026	12203							4325	8772	32843	14128	19691	21932
225	89	4058	1097	12306							4377	8455	32753	13518	19943	23146
200	92	4168	1083	12177							4438	8383	32663	13778	20311	23488
175	86	4299	1146	12176							4504	8410	32582	13943	20681	23660
150	90	4267	1187	12265							4571	8305	32483	13607	21023	22294
125	29	3558	182	3759	100	354	4010	752	1289	11527	4515	7415	30253	15906	21292	21705
100	10	3227	108	4074	308	382	4010	863	1150	11274	4572	7455	30394	15334	21729	21374
75	4.6	3674	135	3648	339	335	3941	882	1137	11521	4582	7417	30413	15319	22000	22168
50	3.2	3727	169	3614	350	334	3902	896	1140	11599	4589	7457	30429	15877	22293	22443
25	3.1	3495	190	3781	359	305	3778	904	1115	11500	4596	7522	30466	14199	22464	21225
5	3.2	3424	185	3828	356	294	3787	902	1112	11527	4593	7515	30476	14177	22570	21292

(b) $SrFe_2As_2$ ($T_N \simeq 195\,K$)

	D_1		D_2		L_{01}			L_{02}			L_1			L_2		
T (K)	$1/\tau_{D,1}$	$\omega_{p,D;1}$	$1/\tau_{D,2}$	$\omega_{p,D;2}$	ω_{01}	γ_{01}	Ω_{01}	ω_{02}	γ_{02}	Ω_{02}	ω_1	γ_1	Ω_1	ω_2	γ_2	Ω_2
295	475	5205	2331	17738							4760	7303	26955	9718	25017	36660
275	432	5312	2324	17633							4733	7277	26965	9687	25095	36636
250	381	5287	2317	17673							4813	7039	27052	10399	25402	36889
225	326	5254	2366	17675							4885	7017	27166	10553	25985	37078
200	294	5075	2354	17699							4932	6895	27442	11154	26393	37057
175	48	2850	340	6964	482	371	2025	1261	1983	15382	5062	6879	29995	13022	24306	36057
150	41	3318	308	6101	480	500	3186	1322	1909	15317	5119	6900	30219	12977	25588	35411
125	38	3543	291	5586	482	495	3737	1376	1855	15383	5054	6349	27297	11197	23999	38812
100	31	3620	285	5252	473	483	4036	1405	1841	15540	5065	6348	27836	11731	23994	38232
75	26	3693	332	5249	482	476	4042	1429	1837	15577	5193	6351	28240	12176	24007	37803
50	20	3720	374	5274	479	470	4062	1445	1827	15573	5198	6360	28482	12424	24026	37620
25	14	3626	359	5179	473	465	4266	1448	1819	15657	5182	6372	28517	12487	24056	37586
5	13	3597	333	5022	469	469	4144	1446	1816	15645	5145	6385	28685	12597	24093	37510

(c) $CaFe_2As_2$ ($T_N \simeq 172\,K$)

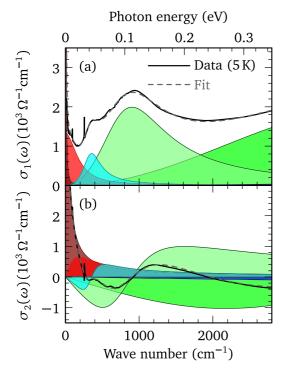|	D_1		D_2		L_{01}			L_{02}			L_1			L_2		
T (K)	$1/\tau_{D,1}$	$\omega_{p,D;1}$	$1/\tau_{D,2}$	$\omega_{p,D;2}$	ω_{01}	γ_{01}	Ω_{01}	ω_{02}	γ_{02}	Ω_{02}	ω_1	γ_1	Ω_1	ω_2	γ_2	Ω_2
295	732	8714	3219	20010							5605	9466	32127	12156	20080	36919
275	646	8485	3151	20040							5766	9470	32864	12560	20097	36119
250	598	8879	3263	20006							5828	9475	33126	12801	20121	35786
225	531	8893	3278	19982							5873	9470	33292	12862	20159	35578
200	491	9029	3122	19332							5843	9488	33925	12958	20216	35345
175	402	8524	2712	18636							5736	9504	34486	12912	20287	35335
150	74	3752	332	6723	667	912	6023	1414	1770	14526	5111	7856	32118	11432	16402	36034
125	55	4084	284	5686	619	919	6112	1488	1765	14910	5288	7835	32694	11832	16330	35332
100	44	4353	304	5207	625	903	6129	1553	1757	15146	5396	7813	32914	12061	16264	35032
75	32	4428	312	4872	623	884	6275	1601	1745	15222	5452	7801	33060	12188	16221	34827
50	21	4530	489	5398	658	854	5748	1643	1733	15294	5526	7792	33200	12325	16200	34615
25	13	4414	497	5428	661	828	5703	1668	1722	15313	5532	7788	33223	12343	16186	34587
5	11	4395	518	5498	661	823	5651	1673	1719	15310	5535	7786	33253	12362	16175	34552

FIG. 2. The comparison of the fit to the complex conductivity of BaFe$_2$As$_2$ at 5 K for light polarized in the planes showing the contributions from the Drude and Lorentz components. (a) The real part of the optical conductivity; note that most of the spectral weight from the narrow Drude component lies outside of the experimental data. (b) The imaginary part of the optical conductivity; note that the response of the narrow Drude component now extends to much higher frequencies, allowing a precise determination of the scattering rate.

The scattering rate for the broad Drude term drops abruptly below T_N, $1/\tau_{D,2} \simeq 1200 \to 190$ cm^{-1}, while the scattering rate for the narrow Drude component drops by over an order of magnitude, $1/\tau_{D,1} \simeq 90 \to 3$ cm^{-1}. As Fig. 1(c) demonstrates, it is rather difficult to determine small values of $1/\tau_D$ from fits to only the real part of the Drude optical conductivity,

$$\sigma_{1,D}(\omega) = \frac{\sigma_0}{1 + \omega^2 \tau_D^2}, \tag{6}$$

which has the form of a Lorentzian centered at zero frequency with a full width at half maximum of $1/\tau_D$ and $\sigma_0 = 2\pi \omega_{p,D}^2 \tau_D / Z_0$. This difficulty is further illustrated in the fit to the data at 5 K in Fig. 2(a), where most of the spectral weight of the narrow Drude component lies below 100 cm^{-1}; if the fit was restricted to only $\sigma_1(\omega)$, the narrow scattering rate would be nearly impossible to determine with any degree of confidence. However, in our analysis the real and imaginary parts of the optical conductivity are fit simultaneously. The imaginary part of the Drude conductivity,

$$\sigma_{2,D}(\omega) = \frac{\sigma_0 \, \omega \tau_D}{1 + \omega^2 \tau_D^2}, \tag{7}$$

is considerably broader than the real part, as Fig. 2(b) indicates, allowing values of $1/\tau_D \lesssim 10$ cm^{-1} to be fit reliably. Thus, despite the loss of free carriers below T_N, the decrease

in the scattering rate for the narrow Drude component is responsible for the increasingly metallic behavior at low temperature [31].

B. SrFe$_2$As$_2$

The temperature dependence of the real part of the optical conductivity for SrFe$_2$As$_2$ ($T_N \simeq 195$ K) for light polarized in the a-b planes is shown in Fig. 3(a) in the infrared region. The overall temperature dependence is quite similar to that of BaFe$_2$As$_2$. Above T_N, the conductivity is metallic and displays little temperature dependence, while below T_N the dramatic narrowing of free-carrier contribution and the decrease in the low-frequency conductivity leads to the redistribution of spectral weight over a much larger energy scale with a prominent peak appearing at $\simeq 1400$ cm^{-1} (the reflectance and the optical conductivity are shown over a broader energy range in Figs. S4 and S5 in the Supplemental Material); however, this feature was observed at a much lower energy, $\simeq 900$ cm^{-1}, in BaFe$_2$As$_2$.

The optical conductivity has been fit using the two-Drude model. The result for the fit just above T_N at 200 K is shown in Fig. 3(b) where it is decomposed into the individual contributions from the Drude and Lorentz components. The free-carrier response is reproduced using a narrow and a broad Drude component, with $\omega_{p,D;1} \simeq 5100$ cm^{-1} and $1/\tau_{D,1} \simeq 300$ cm^{-1}, and $\omega_{p,D;2} \simeq 17\,700$ cm^{-1} and $1/\tau_{D,2} \simeq 2360$ cm^{-1}, respectively, and a series of oscillators at $\omega_1 \simeq 5000$ cm^{-1} and $\omega_2 \simeq 11\,200$ cm^{-1} [Table I(b)]. The plasma frequencies for the Drude components are both larger than what was observed in BaFe$_2$As$_2$, with the combined value for $\omega_p \simeq 18\,400 \pm 600$ cm^{-1}. These results are consistent with other optical studies of this material [31,39].

The fits to the complex conductivity for $T < T_N$ are again performed using the constraint in Eq. (3). The results of the fit at 100 K, shown for the real part of the optical conductivity in Fig. 3(c), indicate that both Drude components decrease in strength and narrow below T_N at the same time that spectral weight is transferred into two new Lorentz oscillators at $\omega_{01} \simeq 470$ cm^{-1} and $\omega_2 \simeq 1450$ cm^{-1} [Table I(b)]. The detailed temperature dependence of the plasma frequencies and scattering rates are shown in Figs. 3(d) and 3(e), respectively. As previously noted, for $T > T_N$, the plasma frequencies display little or no temperature dependence; however, for $T < T_N$, $\omega_{p,D;1} \simeq 5100 \to 3600$ cm^{-1} for the narrow Drude component, while a much larger decrease, $\omega_{p,D;2} \simeq 17\,700 \to 5000$ cm^{-1}, is observed for the broad Drude component. The scattering rate for the narrow Drude component decreases significantly, $1/\tau_{D,1} \simeq 300$ cm^{-1} just above T_N to $\simeq 13$ cm^{-1} at low temperature. The decrease in the scattering rate for the broad Drude component, $1/\tau_{D,2} \simeq 2350 \to 330$ cm^{-1}, while significant, is less dramatic. The total carrier concentration is observed to decrease from $\omega_{p,D} \simeq 18\,400 \to 6200$ cm^{-1}; this $\approx 89\%$ decrease in the number of free carriers for $T \ll T_N$ is somewhat larger than what was observed in BaFe$_2$As$_2$ [31]. The values for the plasma frequencies of the narrow and broad Drude components, and the intensities of the two new oscillators sum to $\omega_p \simeq 17\,320 \pm 600$ cm^{-1} ($T \ll T_N$), indicating that the spectral weight from the narrow and broad Drude components has been almost entirely
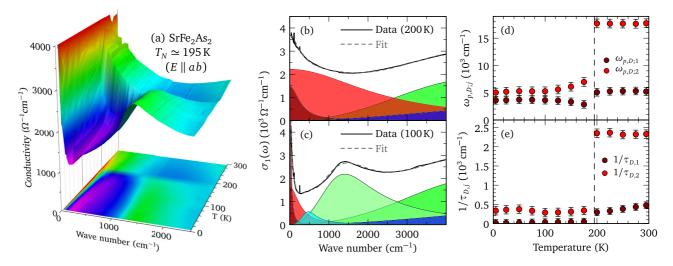
FIG. 3. (a) The temperature dependence of the real part of the optical conductivity for light polarized in the a-b planes of SrFe$_2$As$_2$ above and below $T_N = 195$ K showing the partial gapping of the Fermi surface and the transfer of spectral weight. The fitted individual contributions of the two-Drude model and Lorentz oscillators compared to the real part of the optical conductivity at (b) 200 K and (c) 100 K. The temperature dependence of the (d) plasma frequencies and (e) scattering rates for the two-Drude model above and below T_N.

transferred into the two new oscillators, ω_{01} and ω_{02}. The estimates for the optical gap energies are $\Delta_1 \simeq 58$ meV and $\Delta_2 \simeq 180$ meV, respectively. The value for the large gap is in good agreement with Raman results [62]; however, both of these values are somewhat larger than previous optical estimates [39]. A possible source of uncertainty is that the gap features in this material are much broader than in BaFe$_2$As$_2$, making them more difficult to fit unless controls such as the conservation of spectral weight described in Eq. (3) are introduced.

C. CaFe$_2$As$_2$

The temperature dependence of the real part of the optical conductivity for CaFe$_2$As$_2$ ($T_N \simeq 172$ K) with light polarized

in the a-b planes is shown in Fig. 4(a) in the infrared region. Unlike the previous two materials, the conductivity displays a relatively large temperature dependence above T_N (the reflectance and the optical conductivity are shown over a broader energy range in Figs. S6 and S7 in the Supplemental Material); this is entirely due to the strong temperature dependence of the narrow Drude component and $1/\tau_{D,1}$ [Table I(c)]. Below T_N, there is once again the characteristic narrowing of the free-carrier response coupled with the dramatic suppression of the low-frequency conductivity and the transfer of spectral weight into the peak that emerges at $\simeq 1720$ cm^{-1}.

The result of the fit to the complex conductivity above T_N at 200 K using the two-Drude model is compared to the real part in Fig. 4(b), where it is decomposed into its individual contributions. As in previous cases, the free-carrier
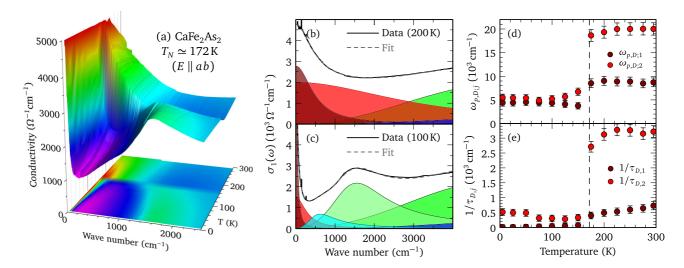

FIG. 4. (a) The temperature dependence of the real part of the optical conductivity for light polarized in the a-b planes of CaFe$_2$As$_2$ above and below T_N showing the partial gapping of the Fermi surface and the transfer of spectral weight. The fitted individual contributions of the two-Drude model and Lorentz oscillators compared to the real part of the optical conductivity at (b) 200 K and (c) 100 K. The temperature dependence of the (d) plasma frequencies and (e) scattering rates for the two-Drude model above and below T_N.

TABLE II. The results for the constrained two-Drude fits to the complex conductivity in AFe$_2$As$_2$ for $A =$ Ba ($T_N \simeq 138$ K), Sr ($T_N \simeq 195$ K), and Ca ($T_N \simeq 172$ K), for $T \gtrsim T_N$, and $T \ll T_N$. The peaks of the two new Lorentz oscillators that appear in the infrared region below T_N, ω_{01} and ω_{02}, are associated with the formation of SDW-like gaps, Δ_1 and Δ_2, respectively. All of these features scale roughly with the Pauling electronegativity, χ_P. All units are in cm^{-1}, except for χ_P and the last two columns.

A	χ_P	$T \gtrsim T_N$				$T \ll T_N$											
		$\omega_{p,D;1}$	$1/\tau_{D,1}$	$\omega_{p,D;2}$	$1/\tau_{D,2}$	$\omega_{p,D;1}$	$1/\tau_{D,1}$	$\omega_{p,D;2}$	$1/\tau_{D,2}$	ω_{01}	γ_{01}	Ω_{01}	ω_{02}	γ_{02}	Ω_{02}	$\Delta_1/k_B T_N$	$\Delta_2/k_B T_N$
Ba	0.89	4210	90	12300	1190	3420	3	3830	190	360	290	3790	900	1110	11530	3.8	9.4
Sr	0.95	5070	290	17700	2350	3600	13	5020	330	470	470	4140	1450	1820	15650	3.5	10.7
Ca	1.00	8520	400	18640	2710	4400	11	5500	518	660	820	5650	1670	1720	15310	5.5	14

response is described quite well by a narrow and a broad Drude component of $\omega_{p,D;1} \simeq 8900$ cm^{-1} and $1/\tau_{D,1} \simeq 490$ cm^{-1}, and $\omega_{p,D;2} \simeq 19\,300$ cm^{-1} and $1/\tau_{D,2} \simeq 3100$ cm^{-1}, and a series of oscillators at $\omega_1 \simeq 5700$ cm^{-1} and $\omega_2 \simeq 12\,800$ cm^{-1} [Table I(c)]. The resulting value of $\omega_p \simeq 21\,200 \pm 1200$ cm^{-1} is larger than was observed in either of the other two materials, in agreement with a previous work [39]. Above T_N, the scattering rate for the broad Drude component has a weak temperature dependence, while the narrow component has a strong temperature dependence, decreasing from $1/\tau_{D,1} \simeq 730$ cm^{-1} at room temperature to $\simeq 400$ cm^{-1} just above T_N [Table I(c)].

Below T_N the two-Drude model is fit to the complex conductivity using the previously described technique. The results of the fit at 100 K, shown for the real part of the optical conductivity in Fig. 4(c), once again show that both Drude components decrease in strength and narrow at the same time that spectral weight is transferred into two new Lorentz oscillators at $\omega_{01} \simeq 660$ cm^{-1} and $\omega_{02} \simeq 1670$ cm^{-1} [Table I(c)]. The detailed temperature dependence of the plasma frequencies and scattering rates are shown in Figs. 4(d) and 4(e), respectively. While the plasma frequencies display little or no temperature dependence for $T > T_N$, below T_N the narrow Drude component decreases somewhat, $\omega_{p,D;1} \simeq 8520 \rightarrow 4400$ cm^{-1}, while a more dramatic decrease, $\omega_{p,D;2} \simeq 18\,640 \rightarrow 5500$ cm^{-1}, is observed for the broad Drude component. The scattering rate for the narrow Drude component decreases dramatically, $1/\tau_{D,1} \simeq 400$ cm^{-1} just above T_N to $\simeq 11$ cm^{-1} at low temperature; the decrease in the scattering rate for the broad Drude component, $1/\tau_{D,2} \simeq 2700 \rightarrow 520$ cm^{-1}, while not as dramatic, is still significant. The total carrier concentration is observed to decrease from $\omega_{p,D} \simeq 21\,200 \rightarrow 7040$ cm^{-1}; this $\approx 89\%$ decrease in the total number of free carriers for $T \ll T_N$ is similar to what was observed in SrFe$_2$As$_2$.

The values for the plasma frequencies of the narrow and broad Drude components, and the intensities of the two new oscillators sum to $\omega_p \simeq 16\,540$ cm^{-1} ($T \ll T_N$), indicating that a significant portion of the spectral weight has been shifted into the two new oscillators, ω_{01} and ω_{02}, leading to estimates for the optical gap energies of $\simeq 82$ and $\simeq 207$ meV, respectively. Both of these values are somewhat larger than previous optical estimates [39], and the value for the large gap is larger than the strong feature observed in the Raman response [63]. However, as in the case of SrFe$_2$As$_2$, the gap features are rather broad, and in the absence of controls, are difficult to fit reliably.

D. Common features

Common to all these materials is the result that above T_N the optical conductivity is reproduced by a strong, broad Drude response that shows little temperature dependence, and a weaker, narrower Drude response where the scattering rate displays a slight temperature dependence. For the progression AFe$_2$As$_2$, for $A =$ Ba, Sr, and Ca, the plasma frequencies for both the narrow and broad Drude components, the scattering rates, and the gaplike features are all increasing (although we would remark that $1/\tau_{D,1}$ and $1/\tau_{D,2}$ are substantially lower in BaFe$_2$As$_2$ than in either of the other two materials). The trends in the electronic properties appear to follow the electronegativity (electron affinity) of the alkaline-earth-metal atoms (Table II). The Pauling electronegativities of Ba, Sr, and Ca are $\chi_P = 0.89$, 0.95 and 1.00, respectively. The increasing electron affinity also leads to a decrease in the covalent radius of 1.98, 1.92, and 1.74 Å, which is also connected to the decreasing c-axis lattice parameter of 13, 12.4, and 11.7 Å for the Ba [20], Sr [25], and Ca [64] materials, respectively. Thus, while the electronegativities of the alkaline-earth-metal atoms are a useful guide for establishing trends in these materials, we would caution that the electronic structure, especially below T_N, is quite complicated, and that detailed structural properties should also be taken into consideration.

In each material, below T_N, despite the appearance of a new structure in the optical conductivity that signals the reconstruction and partial gapping of the Fermi surface, the two-Drude model continues to reproduce the free-carrier response quite well. For the broad Drude component, both the plasma frequency and the scattering rate undergo a significant reduction below T_N, while for the narrow Drude component the plasma frequency decreases only slightly, while the scattering rate decreases by over an order of magnitude. More specifically, $1/\tau_{D,1}$ has a strong temperature dependence below T_N, while $1/\tau_{D,2}$ undergoes an abrupt drop just below T_N, below which it remains relatively constant (Table I). The dramatic collapse of the scattering rate for the narrow Drude component for $T \ll T_N$ is reminiscent of what is observed in other materials where a Fermi surface reconstruction leads to large portions of the Fermi surface being removed, with a concomitant loss of free carriers; in some special cases this is referred to as a "nodal metal" [65–67], but more generally it describes any semimetal with a very small Fermi surface. In multiband materials, it is not uncommon for one (or more) of the scattering rates to be quite small, typically on the order of several cm^{-1} [68,69]. The very small values of $1/\tau_{D,1}$ at low temperatures is similar to what is seen in some Weyl and

Dirac semimetals, where scattering rates are only a few cm^{-1} [70–72]; indeed, the observation [47] and calculation [60] of Dirac conelike dispersion of the electronic bands of BaFe$_2$As$_2$ below T_N suggests that this is a natural comparison.

In all three materials, a structure is observed in the optical conductivity that is associated with the partial gapping of the Fermi surface that appears below T_N, a small gap (Δ_1) and a large gap (Δ_2); these features may be associated transitions between relatively flat bands located at high-symmetry points (Γ and M') [60]. The values range from $\Delta_1 \simeq 44$–82 meV for the small gap to $\Delta_2 \simeq 112$–207 meV for the large gap. This yields values of $\Delta_1/k_B T_N \simeq 3.8$–5.5 and $\Delta_2/k_B T_N \simeq 9.4$–14, where k_B is Boltzmann's constant. As previously noted, both Δ_1 and Δ_2 are increasing across this family of materials; however, the ratio of the gaps shows little variation, with $\Delta_2/\Delta_1 \simeq 2.5$–3, suggesting that the gaps scale with the electronic bandwidth.

IV. CONCLUSIONS

The temperature dependence of the detailed optical properties of BaFe$_2$As$_2$, SrFe$_2$As$_2$, and CaFe$_2$As$_2$ single crystals have been determined over a wide energy range above and below $T_N \simeq 138$, 195, and 172 K, respectively, for light polarized in the a-b planes. The complex optical properties may be reliably fit using two Drude components in combination with a series of Lorentz oscillators. Above T_N in all three materials, the free-carrier response consists of a weak, narrow Drude term, and a much stronger, broader Drude term, both of which display only a weak temperature dependence. The plasma frequencies of both the narrow and broad terms are observed to increase in the Ba, Sr, and Ca family of materials. Below T_N the Fermi surface reconstruction produces dramatic changes in the complex conductivity. While the materials are increasingly metallic at low temperature, there is a decrease in the low-frequency spectral weight from both the narrow and broad Drude components and a commensurate transfer to the gaplike features (Δ_1 and Δ_2) observed at higher energies. The complex conductivity may only be reliably fit using the two-Drude model if the constraint that the spectral weight is constant below roughly 5000 cm^{-1} is introduced. The loss of spectral weight from the narrow Drude component is apparently transferred to peak in the optical conductivity associated with the low-energy gap Δ_1, while the loss of spectral weight from the broad Drude component is apparently transferred to the high-energy gap Δ_2.

Below T_N, both the plasma frequency and the scattering rate in the broad Drude term decrease substantially; the plasma frequency in the narrow Drude term experiences a slight decrease, but the scattering rate decreases by over an order of magnitude, and in the case of BaFe$_2$As$_2$, is only a few cm^{-1} for $T \ll T_N$. Dirac semimetals often display extremely small scattering rates, suggesting that the extraordinarily low value for the scattering rate in these materials may be related to the Dirac conelike dispersion observed in the electronic bands below T_N.

[1] D. C. Johnston, The puzzle of high temperature superconductivity in layered iron pnictides and chalcogenides, Adv. Phys. **59**, 803 (2010).

[2] J. Paglione and R. L. Greene, High-temperature superconductivity in iron-based materials, Nat. Phys. **6**, 645 (2010).

[3] P. C. Canfield and S. L. Bud'ko, FeAs-based superconductivity: A case study of the effects of transition metal doping on BaFe$_2$As$_2$, Ann. Rev. Condens. Matter Phys. **1**, 27 (2010).

[4] Q. Si, R. Yu, and E. Abrahams, High-temperature superconductivity in iron pnictides and chalcogenides, Nat. Rev. Mater. **1**, 16017 (2016).

[5] F. Ishikawa, N. Eguchi, M. Kodama, K. Fujimaki, M. Einaga, A. Ohmura, A. Nakayama, A. Mitsuda, and Y. Yamada, Zero-resistance superconducting phase in BaFe$_2$As$_2$ under high pressure, Phys. Rev. B **79**, 172506 (2009).

[6] P. L. Alireza, Y. T. Chris Ko, J. Gillett, C. M. Petrone, J. M. Cole, S. E. Sebastian, and G. G. Lonzarich, Superconductivity up to 29 K in SrFe$_2$As$_2$ and BaFe$_2$As$_2$ at high pressures, J. Phys: Condens. Matter **21**, 012208 (2009).

[7] E. Colombier, S. L. Bud'ko, N. Ni, and P. C. Canfield, Complete pressure-dependent phase diagrams for SrFe$_2$As$_2$ and BaFe$_2$As$_2$, Phys. Rev. B **79**, 224518 (2009).

[8] T. Yamazaki, N. Takeshita, R. Kobayashi, H. Fukazawa, Y. Kohori, K. Kihou, C.-H. Lee, H. Kito, A. Iyo, and H. Eisaki, Appearance of pressure-induced superconductivity in BaFe$_2$As$_2$ under hydrostatic conditions and its extremely high sensitivity to uniaxial stress, Phys. Rev. B **81**, 224511 (2010).

[9] A. S. Sefat, R. Jin, M. A. McGuire, B. C. Sales, D. J. Singh, and D. Mandrus, Superconductivity at 22 K in Co-Doped BaFe$_2$As$_2$ Crystals, Phys. Rev. Lett. **101**, 117004 (2008).

[10] N. Ni, M. E. Tillman, J.-Q. Yan, A. Kracher, S. T. Hannahs, S. L. Bud'ko, and P. C. Canfield, Effects of Co substitution on thermodynamic and transport properties and anisotropic H_{c2} in Ba(Fe$_{1-x}$Co$_x$)$_2$As$_2$ single crystals, Phys. Rev. B **78**, 214515 (2008).

[11] J.-H. Chu, J. G. Analytis, C. Kucharczyk, and I. R. Fisher, Determination of the phase diagram of the electron-doped superconductor Ba(Fe$_{1-x}$Co$_x$)$_2$As$_2$, Phys. Rev. B **79**, 014506 (2009).

[12] P. C. Canfield, S. L. Bud'ko, N. Ni, J. Q. Yan, and A. Kracher, Decoupling of the superconducting and magnetic/structural phase transitions in electron-doped BaFe$_2$As$_2$, Phys. Rev. B **80**, 060501 (2009).

[13] M. Rotter, M. Tegel, and D. Johrendt, Superconductivity at 38 K in the Iron Arsenide (Ba$_{1-x}$K$_x$)Fe$_2$As$_2$, Phys. Rev. Lett. **101**, 107006 (2008).

[14] M. S. Torikachvili, S. L. Bud'ko, N. Ni, and P. C. Canfield, Effect of pressure on the structural phase transition and superconductivity in (Ba$_{1-x}$K$_x$)Fe$_2$As$_2$ ($x = 0$ and 0.45) and SrFe$_2$As$_2$ single crystals, Phys. Rev. B **78**, 104527 (2008).

[15] H. Chen, Y. Ren, Y. Qiu, W. Bao, R. H. Liu, G. Wu, T. Wu, Y. L. Xie, X. F. Wang, Q. Huang, and X. H. Chen, Coexistence of the spin-density wave and superconductivity in Ba$_{1-x}$K$_x$Fe$_2$As$_2$, Europhys. Lett. **85**, 17006 (2009).

[16] S. Jiang, H. Xing, G. Xuan, C. Wang, Z. Ren, C. Feng, J. Dai, Z. Xu, and G. Cao, Superconductivity up to 30 K in the vicinity of the quantum critical point in BaFe$_2$(As$_{1-x}$P$_x$)$_2$, J. Phys.: Condens. Matter **21**, 382203 (2009).

[17] F. Rullier-Albenque, D. Colson, A. Forget, P. Thuéry, and S. Poissonnet, Hole and electron contributions to the transport properties of Ba(Fe$_{1-x}$Ru$_x$)$_2$As$_2$ single crystals, Phys. Rev. B **81**, 224503 (2010).

[18] A. Thaler, N. Ni, A. Kracher, J. Q. Yan, S. L. Bud'ko, and P. C. Canfield, Physical and magnetic properties of Ba(Fe$_{1-x}$Ru$_x$)$_2$As$_2$ single crystals, Phys. Rev. B **82**, 014534 (2010).

[19] Y. Nakai, T. Iye, S. Kitagawa, K. Ishida, H. Ikeda, S. Kasahara, H. Shishido, T. Shibauchi, Y. Matsuda, and T. Terashima, Unconventional Superconductivity and Antiferromagnetic Quantum Critical Behavior in the Isovalent-Doped BaFe$_2$(As$_{1-x}$P$_x$)$_2$, Phys. Rev. Lett. **105**, 107003 (2010).

[20] M. Rotter, M. Tegel, D. Johrendt, I. Schellenberg, W. Hermes, and R. Pöttgen, Spin-density-wave anomaly at 140 K in the ternary iron arsenide BaFe$_2$As$_2$, Phys. Rev. B **78**, 020503(R) (2008).

[21] X. F. Wang, T. Wu, G. Wu, H. Chen, Y. L. Xie, J. J. Ying, Y. J. Yan, R. H. Liu, and X. H. Chen, Anisotropy in the Electrical Resistivity and Susceptibility of Superconducting BaFe$_2$As$_2$ Single Crystals, Phys. Rev. Lett. **102**, 117005 (2009).

[22] I. R. Fisher, L. Degiorgi, and Z. X. Shen, In-plane electronic anisotropy of underdoped "122" Fe-arsenide superconductors revealed by measurements of detwinned single crystals, Rep. Prog. Phys. **74**, 124506 (2011).

[23] J.-H. Chu, J. G. Analytis, K. De Greve, P. L. McMahon, Z. Islam, Y. Yamamoto, and I. R. Fisher, In-plane resistivity anisotropy in an underdoped iron arsenide superconductor, Science **329**, 824 (2010).

[24] S. Ishida, M. Nakajima, T. Liang, K. Kihou, C. H. Lee, A. Iyo, H. Eisaki, T. Kakeshita, Y. Tomioka, T. Ito, and S. Uchida, Anisotropy of the In-Plane Resistivity of Underdoped Ba(Fe$_{1-x}$Co$_x$)$_2$As$_2$ Superconductors Induced by Impurity Scattering in the Antiferromagnetic Orthorhombic Phase, Phys. Rev. Lett. **110**, 207001 (2013).

[25] M. Tegel, M. Rotter, V. Weiß, F. M Schappacher, R. Pöttgen, and D. Johrendt, Structural and magnetic phase transitions in the ternary iron arsenides SrFe$_2$As$_2$ and EuFe$_2$As$_2$, J. Phys.: Condens. Matter **20**, 452201 (2008).

[26] J. Zhao, W. Ratcliff, J. W. Lynn, G. F. Chen, J. L. Luo, N. L. Wang, J. Hu, and P. Dai, Spin and lattice structures

[27] A. I. Goldman, D. N. Argyriou, B. Ouladdiaf, T. Chatterji, A. Kreyssig, S. Nandi, N. Ni, S. L. Bud'ko, P. C. Canfield, and R. J. McQueeney, Lattice and magnetic instabilities in CaFe$_2$As$_2$: A single-crystal neutron diffraction study, Phys. Rev. B **78**, 100506 (2008).

[28] M. A. Tanatar, N. Ni, G. D. Samolyuk, S. L. Bud'ko, P. C. Canfield, and R. Prozorov, Resistivity anisotropy of AFe$_2$As$_2$ ($A =$ Ca, Sr, Ba): Direct versus Montgomery technique measurements, Phys. Rev. B **79**, 134528 (2009).

[29] M. A. Tanatar, E. C. Blomberg, A. Kreyssig, M. G. Kim, N. Ni, A. Thaler, S. L. Bud'ko, P. C. Canfield, A. I. Goldman, I. I. Mazin, and R. Prozorov, Uniaxial-strain mechanical detwinning of CaFe$_2$As$_2$ and BaFe$_2$As$_2$ crystals: Optical and transport study, Phys. Rev. B **81**, 184508 (2010).

[30] E. C. Blomberg, M. A. Tanatar, A. Kreyssig, N. Ni, A. Thaler, R. Hu, S. L. Bud'ko, P. C. Canfield, A. I. Goldman, and R. Prozorov, In-plane anisotropy of electrical resistivity in strain-detwinned SrFe$_2$As$_2$, Phys. Rev. B **83**, 134505 (2011).

[31] W. Z. Hu, J. Dong, G. Li, Z. Li, P. Zheng, G. F. Chen, J. L. Luo, and N. L. Wang, Origin of the Spin Density Wave Instability in AFe$_2$As$_2$ ($A =$ Ba, Sr) as Revealed by Optical Spectroscopy, Phys. Rev. Lett. **101**, 257005 (2008).

[32] A. Akrap, J. J. Tu, L. J. Li, G. H. Cao, Z. A. Xu, and C. C. Homes, Infrared phonon anomaly in BaFe$_2$As$_2$, Phys. Rev. B **80**, 180502 (2009).

[33] F. Pfuner, J. G. Analytis, J.-H. Chu, I. R. Fisher, and L. Degiorgi, Charge dynamics of the spin-density-wave state in BaFe$_2$As$_2$, Eur. Phys. J. B **67**, 513 (2009).

[34] Z. G. Chen, T. Dong, R. H. Ruan, B. F. Hu, B. Cheng, W. Z. Hu, P. Zheng, Z. Fang, X. Dai, and N. L. Wang, Measurement of the c-Axis Optical Reflectance of AFe$_2$As$_2$ ($A =$ Ba, Sr) Single Crystals: Evidence of Different Mechanisms for the Formation of Two Energy Gaps, Phys. Rev. Lett. **105**, 097003 (2010).

[35] A. A. Schafgans, B. C. Pursley, A. D. LaForge, A. S. Sefat, D. Mandrus, and D. N. Basov, Phonon splitting and anomalous enhancement of infrared-active modes in BaFe$_2$As$_2$, Phys. Rev. B **84**, 052501 (2011).

[36] S. J. Moon, A. A. Schafgans, S. Kasahara, T. Shibauchi, T. Terashima, Y. Matsuda, M. A. Tanatar, R. Prozorov, A. Thaler, P. C. Canfield, A. S. Sefat, D. Mandrus, and D. N. Basov, Infrared Measurement of the Pseudogap of P-Doped and Co-Doped High-Temperature BaFe$_2$As$_2$ Superconductors, Phys. Rev. Lett. **109**, 027006 (2012).

[37] M. Nakajima, T. Liang, S. Ishida, Y. Tomioka, K. Kihou, C. H. Lee, A. Iyo, H. Eisaki, T. Kakeshita, T. Ito, and S. Uchida, Unprecedented anisotropic metallic state in undoped iron arsenide BaFe$_2$As$_2$ revealed by optical spectroscopy, Proc. Natl. Acad. Sci. U.S.A. **108**, 12238 (2011).

[38] A. Dusza, A. Lucarelli, F. Pfuner, J.-H. Chu, I. R. Fisher, and L. Degiorgi, Anisotropic charge dynamics in detwinned Ba(Fe$_{1-x}$Co$_x$)$_2$As$_2$, Europhys. Lett. **93**, 37002 (2011).

[39] A. Charnukha, D. Pröpper, T. I. Larkin, D. L. Sun, Z. W. Li, C. T. Lin, T. Wolf, B. Keimer, and A. V. Boris, Spin-density-wave-induced anomalies in the optical conductivity of AFe$_2$As$_2$, ($A =$ Ca, Sr, Ba) single-crystalline iron pnictides, Phys. Rev. B **88**, 184511 (2013).

[40] M. Nakajima, S. Ishida, T. Tanaka, K. Kihou, Y. Tomioka, T. Saito, C. H. Lee, H. Fukazawa, Y. Kohori, T. Kakeshita, A. Iyo,

of single-crystalline SrFe$_2$As$_2$, Phys. Rev. B **78**, 140504 (2008).

T. Ito, H. Eisaki, and S. Uchida, Normal-state charge dynamics in doped BaFe$_2$As$_2$: Roles of doping and necessary ingredients for superconductivity, Sci. Rep. **4**, 5873 (2014).

[41] X. B. Wang, H. P. Wang, T. Dong, R. Y. Chen, and N. L. Wang, Optical spectroscopy study of the collapsed tetragonal phase of CaFe$_2$(As$_{0.935}$P$_{0.065}$)$_2$ single crystals, Phys. Rev. B **90**, 144513 (2014).

[42] D. J. Singh, Electronic structure and doping in BaFe$_2$As$_2$ and LiFeAs: Density functional calculations, Phys. Rev. B **78**, 094511 (2008).

[43] J. Fink, S. Thirupathaiah, R. Ovsyannikov, H. A. Dürr, R. Follath, Y. Huang, S. de Jong, M. S. Golden, Y.-Z. Zhang, H. O. Jeschke, R. Valentí, C. Felser, S. D. Farahani, M. Rotter, and D. Johrendt, Electronic structure studies of BaFe$_2$As$_2$ by angle-resolved photoemission spectroscopy, Phys. Rev. B **79**, 155118 (2009).

[44] D. Wu, N. Barišić, P. Kallina, A. Faridian, B. Gorshunov, N. Drichko, L. J. Li, X. Lin, G. H. Cao, Z. A. Xu, N. L. Wang, and M. Dressel, Optical investigations of the normal and superconducting states reveal two electronic subsystems in iron pnictides, Phys. Rev. B **81**, 100512(R) (2010).

[45] M. Yi, D. H. Lu, J. G. Analytis, J.-H. Chu, S.-K. Mo, R.-H. He, M. Hashimoto, R. G. Moore, I. I. Mazin, D. J. Singh, Z. Hussain, I. R. Fisher, and Z.-X. Shen, Unconventional electronic reconstruction in undoped (Ba,Sr)Fe$_2$As$_2$ across the spin density wave transition, Phys. Rev. B **80**, 174510 (2009).

[46] L. X. Yang *et al.*, Electronic Structure and Unusual Exchange Splitting in the Spin-Density-Wave State of the BaFe$_2$As$_2$ Parent Compound of Iron-Based Superconductors, Phys. Rev. Lett. **102**, 107002 (2009).

[47] P. Richard, K. Nakayama, T. Sato, M. Neupane, Y.-M. Xu, J. H. Bowen, G. F. Chen, J. L. Luo, N. L. Wang, X. Dai, Z. Fang, H. Ding, and T. Takahashi, Observation of Dirac Cone Electronic Dispersion in BaFe$_2$As$_2$, Phys. Rev. Lett. **104**, 137001 (2010).

[48] T. Shimojima, K. Ishizaka, Y. Ishida, N. Katayama, K. Ohgushi, T. Kiss, M. Okawa, T. Togashi, X.-Y. Wang, C.-T. Chen, S. Watanabe, R. Kadota, T. Oguchi, A. Chainani, and S. Shin, Orbital-Dependent Modifications of Electronic Structure across the Magnetostructural Transition in BaFe$_2$As$_2$, Phys. Rev. Lett. **104**, 057002 (2010).

[49] M. Fuglsang Jensen, V. Brouet, E. Papalazarou, A. Nicolaou, A. Taleb-Ibrahimi, P. L. Fèvre, F. Bertran, A. Forget, and D. Colson, Angle-resolved photoemission study of the role of nesting and orbital orderings in the antiferromagnetic phase of BaFe$_2$As$_2$, Phys. Rev. B **84**, 014509 (2011).

[50] R. S. Dhaka, R. Jiang, S. Ran, S. L. Bud'ko, P. C. Canfield, B. N. Harmon, A. Kaminski, M. Tomić, R. Valentí, and Y. Lee, Dramatic changes in the electronic structure upon transition to the collapsed tetragonal phase in CaFe$_2$As$_2$, Phys. Rev. B **89**, 020511 (2014).

[51] K. Gofryk, B. Saparov, T. Durakiewicz, A. Chikina, S. Danzenbächer, D. V. Vyalikh, M. J. Graf, and A. S. Sefat, Fermi-Surface Reconstruction and Complex Phase Equilibria in CaFe$_2$As$_2$, Phys. Rev. Lett. **112**, 186401 (2014).

[52] J.-Q. Yan, A. Kreyssig, S. Nandi, N. Ni, S. L. Bud'ko, A. Kracher, R. J. McQueeney, R. W. McCallum, T. A. Lograsso, A. I. Goldman, and P. C. Canfield, Structural transition and anisotropic properties of single-crystalline SrFe$_2$As$_2$, Phys. Rev. B **78**, 024516 (2008).

[53] N. Ni, S. Nandi, A. Kreyssig, A. I. Goldman, E. D. Mun, S. L. Bud'ko, and P. C. Canfield, First-order structural phase transition in CaFe$_2$As$_2$, Phys. Rev. B **78**, 014523 (2008).

[54] C. C. Homes, M. Reedyk, D. A. Crandles, and T. Timusk, Technique for measuring the reflectance of irregular, submillimeter-sized samples, Appl. Opt. **32**, 2976 (1993).

[55] M. Dressel and G. Grüner, *Electrodynamics of Solids* (Cambridge University Press, Cambridge, 2001).

[56] F. Wooten, *Optical Properties of Solids* (Academic, New York, 1972), pp. 244–250.

[57] See Supplemental Material at http://link.aps.org/supplemental/10.1103/PhysRevB.94.195142 for the temperature dependence of the reflectance and the real part of the optical conductivity shown over a wide frequency range, as well as a more detailed examination of the spectral weight.

[58] B. Valenzuela, M. J. Calderón, G. León, and E. Bascones, Optical conductivity and Raman scattering of iron superconductors, Phys. Rev. B **87**, 075136 (2013).

[59] M. J. Calderón, L. de' Medici, B. Valenzuela, and E. Bascones, Correlation, doping, and interband effects on the optical conductivity of iron superconductors, Phys. Rev. B **90**, 115128 (2014).

[60] Z. P. Yin, K. Haule, and G. Kotliar, Magnetism and charge dynamics in iron pnictides, Nat. Phys. **7**, 294 (2011).

[61] L. Chauvière, Y. Gallais, M. Cazayous, M. A. Méasson, A. Sacuto, D. Colson, and A. Forget, Raman scattering study of spin-density-wave order and electron-phonon coupling in Ba(Fe$_{1-x}$Co$_x$)$_2$As$_2$, Phys. Rev. B **84**, 104508 (2011).

[62] Y.-X. Yang, Y. Gallais, F. Rullier-Albenque, M.-A. Méasson, M. Cazayous, A. Sacuto, J. Shi, D. Colson, and A. Forget, Temperature-induced change in the Fermi surface topology in the spin density wave phase of Sr(Fe$_{1-x}$Co$_x$)$_2$As$_2$, Phys. Rev. B **89**, 125130 (2014).

[63] W.-L. Zhang, Z. P. Yin, A. Ignatov, Z. Bukowski, J. Karpinski, A. S. Sefat, H. Ding, P. Richard, and G. Blumberg, Raman scattering study of spin-density-wave-induced anisotropic electronic properties in AFe$_2$As$_2$ (A = Ca, Eu), Phys. Rev. B **93**, 205106 (2016).

[64] G. Wu, H. Chen, T. Wu, Y. L. Xie, Y. J. Yan, R. H. Liu, X. F. Wang, J. J. Ying, and X. H. Chen, Different resistivity response to spin-density wave and superconductivity at 20 K in Ca$_{1-x}$Na$_x$Fe$_2$As$_2$, J. Phys.: Condens. Matter **20**, 422201 (2008).

[65] Y. Ando, A. N. Lavrov, S. Komiya, K. Segawa, and X. F. Sun, Mobility of the Doped Holes and the Antiferromagnetic Correlations in Underdoped High-T_c Cuprates, Phys. Rev. Lett. **87**, 017001 (2001).

[66] Y. S. Lee, K. Segawa, Z. Q. Li, W. J. Padilla, M. Dumm, S. V. Dordevic, C. C. Homes, Y. Ando, and D. N. Basov, Electrodynamics of the nodal metal state in weakly doped high-T_c cuprates, Phys. Rev. B **72**, 054529 (2005).

[67] C. C. Homes, J. J. Tu, J. Li, G. D. Gu, and A. Akrap, Optical conductivity of nodal metals, Sci. Rep. **3**, 3446 (2013).

[68] C. C. Homes, Y. M. Dai, J. S. Wen, Z. J. Xu, and G. D. Gu, FeTe$_{0.55}$Se$_{0.45}$: A multiband superconductor in the clean and dirty limit, Phys. Rev. B **91**, 144503 (2015).

[69] C. C. Homes, M. N. Ali, and R. J. Cava, Optical properties of the perfectly compensated semimetal WTe$_2$, Phys. Rev. B **92**, 161109(R) (2015).

[70] R. Y. Chen, S. J. Zhang, J. A. Schneeloch, C. Zhang, Q. Li, G. D. Gu, and N. L. Wang, Optical spectroscopy study of the three-dimensional Dirac semimetal ZrTe$_5$, Phys. Rev. B **92**, 075107 (2015).

[71] B. Xu, Y. M. Dai, L. X. Zhao, K. Wang, R. Yang, W. Zhang, J. Y. Liu, H. Xiao, G. F. Chen, A. J. Taylor, D. A. Yarotski, R. P. Prasankumar, and X. G. Qiu, Optical spectroscopy of the Weyl semimetal TaAs, Phys. Rev. B **93**, 121110 (2016).

[72] A. Akrap *et al.*, Magneto-Optical Signature of Massless Kane Electrons in Cd$_3$As$_2$, Phys. Rev. Lett. **117**, 136401 (2016).